International Journal of Hydrogen Energy 80 (2024) 137–150

Contents lists available at ScienceDirect

International Journal of Hydrogen Energy

journal homepage: www.elsevier.com/locate/he

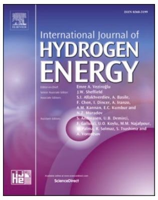

Elucidating the local structure and electronic properties of a highly active overall alkaline water splitting $Ni_xCo_{1-x}O$/hollow carbon sphere catalyst

Victor Mashindi [a], Maxwell W. Terban [b], Debora Motta Meira [c], Beatriz D. Moreno [c], Prettier Morongoa [d], Rirhandzu Rikhotso-Mbungela [d], Geneve've Marx [e], Jaco Olivier [e], Dean H. Barrett [a,*], Nosipho Moloto [a]

[a] *Molecular Sciences Institute, School of Chemistry, University of the Witwatersrand, Johannesburg, South Africa*
[b] *Max Planck Institute for Solid State Research, Heisenbergstraße 1, 70569, Stuttgart, Germany*
[c] *Canadian Light Source Inc., 44 Innovation Boulevard, Saskatoon, SK, S7N 2V3, Canada*
[d] *Council for Scientific and Industrial Research, Brumeria, South Africa*
[e] *Centre for High-Resolution Transmission Electron Microscopy, Nelson Mandela University, South Africa*

A R T I C L E I N F O

Keywords:
Bimetallic transition metal oxide
Overall water splitting
PDF-Total scattering
EXAFS
Electronic modification

A B S T R A C T

A $Ni_xCo_{1-x}O$/HCS catalyst with superior water-splitting is presented. High water-splitting reaction kinetics and enhanced durability were observed. The structure-function relationship was investigated with XPS, which demonstrated the presence of dominant Ni^{2+} and Co^{2+} species and a functionalized HCS support where nucleation of small metal oxide nanoparticles occurred. The PDF showed broadened Nickel/Cobalt-oxide bonds and expansion of the metal-metal pair distances. The alteration of the Metal-Oxide and Metal-Metal-Oxide bonds favored better HER and OER electrocatalysis, also as supported by DFT. EXAFS showed the existence of the bimetallic oxide catalyst and the stretching of the Ni–O bonds due to the coordination of the Ni–O with the Co. The composite exhibited higher activity and enhanced electrocatalytic mechanism towards water splitting through higher exchange current densities (0.615 and 0.886 mA cm^{-2}) and low charge transfer resistance (14 and 10 Ω) respectively. Chronoamperometry proved the catalyst's stability during prolonged electrolysis.

1. Introduction

Fossil fuels dominate as the primary energy source powering the global economy. However, the combustion of fossil fuels and the resulting gaseous emissions contribute to pollution and are an increasingly limited resource. Momentum toward embracing renewable and sustainable energy systems has grown in recent decades. One such renewable energy source, hydrogen, has garnered significant attention due to its abundance and high energy density. Hydrogen also serves as an excellent energy carrier, and its involvement in electrochemical processes offers an alternative, sustainable, and environmentally friendly energy solution [1].

When applied in hydrogen-based fuel cells, a catalyst facilitates the electrolysis of hydrogen and oxygen, enabling oxygen reduction and hydrogen oxidation reactions. These processes generate clean electricity, produce minimal heat, and leave behind only water as a byproduct [2]. When hydrogen is derived from clean and environmentally friendly methods, the carbon footprint can be reduced to zero [3]. This can be achieved via the electrolysis of acidified or alkaline water, enabling clean hydrogen and oxygen production with minimal energy expenditure. However, these processes rely on expensive and rare platinum catalysts for the hydrogen evolution reaction (HER) or iridium and ruthenium oxides for the oxygen evolution reaction (OER) presenting a significant challenge to large-scale production. Therefore, the development of efficient catalysts and processes that employ more affordable, abundant, and electrocatalytically active materials for both the OER and HER is critically important.

Monometallic and bimetallic transition metal composites demonstrate promising activity in both HER and OER, particularly in alkaline environments [4–6]. However, most of these materials suffer from slower activation kinetics and higher overpotential compared to platinum group metal-based catalysts currently employed. To mitigate the challenge of poor electrocatalysis from the monometallic catalysts, significant research has focused on bimetallic and trimetallic oxide

---

* Corresponding author.
E-mail address: Dean.Barrett1@wits.ac.za (D.H. Barrett).

https://doi.org/10.1016/j.ijhydene.2024.07.122
Received 17 April 2024; Received in revised form 11 June 2024; Accepted 8 July 2024
Available online 15 July 2024

composites for the overall alkaline water-splitting reactions. Significant improvements in alkaline electrocatalysis have been prominently observed, mostly due to the synergistic effects arising from the electronic interaction between the two- or three-metal oxides [7] or the changes in the surface properties of the catalysts due to lattice strain, which often affects the interaction of the reaction intermediates of the HER or OER with the catalyst's active sites [8]. Though a huge body of bimetallic and trimetallic transition metal oxides applied in overall alkaline water splitting exists, a thorough understanding of how underlying structure drives functionality in many cases remains undeveloped.

In this study, we present a simplified and reproducible method for synthesizing a bimetallic $Ni_xCo_{1-x}O$/HCS composite catalyst. Furthermore, we elucidated the local structure and electronic properties of the catalyst and concluded the proposed structure to functionality properties in overall alkaline water splitting. This composite exhibits excellent performance in overall water-splitting, excelling in both the OER and HER with an overall cell voltage of 1.68 V. The catalyst showcased faster kinetics than the monometallic counterparts for the HER with a Tafel slope of 68.2 $mVdec^1$ and an overpotential of 178 mV at a current density of 10 $mAcm^{-2}$. In OER, a lower overpotential of 276.4 mV was observed at a current density of 10 $mAcm^-$,^{2} coupled with a Tafel slope of 52.1 $mVdec^{-1}$. For at least 16 h of chronoamperometry at the OER and HER overpotential, the catalyst demonstrated significant durability achieving higher current density at the end of the cycle than the initial current density, suggesting catalyst modification and exposure of more catalytic active sites during the electrochemical process. The new catalyst demonstrated high exchange current density, and enhanced activity and durability compared to monometallic NiO/HCS, CoO/HCS, and other state-of-the-art catalysts reported for these reactions. The HRTEM coupled with EELS and SAED demonstrated the uniform distribution of the bimetallic oxide nanoparticles on the supports and the existence of larger nanoparticles, 10–50 nm in diameter which are metallic with a graphitic carbon shell around them. The second is smaller nanoparticles 1–5 nm in diameter which are homogenously distributed over the oxy-carbon shell of the support. These smaller nanoparticles are likely oxide but not crystalline everywhere. The SAED patterns also showed the expansion of the Ni (111) plane due to the compositing effect between the Ni and Co oxides. The total scattering pair distribution function and EXAFS data demonstrated the elongation of the M − O (Ni, Co – O) bond and surface strain possibly due to the Co doping into the Ni – O structure. This could have favored faster and thermodynamically feasible adsorption of intermediates and desorption of H_2 and O_2 compared to the undisturbed monometallic composites. Herein, we delved deeper into the structural, electronic, and molecular properties of this $Ni_xCo_{1-x}O$/HCS composite as we investigated the catalyst's structure-function properties.

2. Experimental

2.1. Chemicals

Tris(acetylacetonate)cobalt(III) [$Co(acac)_3$, 99.99%], nickel(II)bis (acetylacetonate [$Ni(acac)_2$, 95%] tetraethyl orthosilicate (TEOS, 98%), resorcinol, formaldehyde (37%), absolute ethanol (EtOH,99.9%) hydrofluoric acid (HF,48%), cetyltrimethylammonium bromide (CTAB), potassium hydroxide pellets (KOH), nickel foam and Nafion perfluorinated resin solution (5 wt% in water) were all purchased from Sigma-Aldrich and used as received. Ammonia solution (25%, Associated Chemical Enterprises), isopropyl alcohol (99.6%, MK chemicals) ultrapure water (DI, 18.2 MΩ cm, Merck Millipore), alumina polish (0.05 and 0.1 μm and polishing cloths, Buehler) and argon gas (99.99%, Afrox SA), nitrogen gas (99.99%, Afrox SA), hydrogen-oxygen-nitrogen special gas for GC (5%, 10% and 30% H_2 and balance N_2, Afrox), (5%, 10% and 30% O_2 and balance N_2, Afrox SA) were sourced and used as received without further purification. The Fumasep FAA-3-50 membrane was ordered from the Fuel Cell Store and sections were used as delivered.

2.2. Synthesis of $Ni_xCo_{1-x}O$/HCS

A silica template was used for the preparation of hollow carbon spheres (HCS). The HCS were used as support for the bimetallic oxide composites. The silica template and HCS were prepared similarly to a method we previously reported [9]. The detailed methodology for the silica and HCS synthesis is provided in the supplementary information. To prepare a 30 wt% $Ni_xCo_{1-x}O$/HCS catalyst, the $Co(acac)_3$ (129.6 mg) and $Ni(acac)_2$ (93.8 mg) were thoroughly mixed with HCS (100 mg) in a ceramic crucible. The mixture was annealed in a tubular horizontal furnace under a steady argon stream at 20 mL. min^{-1}. Initially, the furnace was heated to 100 °C and held isothermally for 30 min followed by a further ramping step until 350 °C at a heating rate of 2.5 °C.min^{-1}. The reaction proceeded for an additional 2 h followed by natural cooling and harvesting of the product, $Ni_xCo_{1-x}O$/HCS.

2.3. Materials characterization

The morphology of the catalysts was investigated with transmission electron microscopy (TEM) coupled to energy-dispersive x-ray spectroscopy (EDS) on a JEOL JEM-2100 microscope operating at 200 kV. Further TEM analysis was performed using a double-aberration corrected JEOL JEM-ARM 200F operated at 200 kV and equipped with an Oxford Xmax 100 energy dispersive spectroscopy (EDS) detector and Gatan GIP 965ERS with dual electron-energy loss spectroscopy (EELS) capability. Imaging and analysis of the samples were done in TEM using parallel illumination and scanning mode (STEM), using a sub-angstrom-sized probe with a probe current between 68 pA and 281 pA. These conditions ensured optimal beam current while minimizing the risk of beam damage to the specimen. The probe convergence semi-angle used was fixed at 23 mrad with acceptance semi-angles of 84 mrad (GIF) and 34–137 mrad (dark-field detector). The BF detector acceptance semi-angle was set at 0–12 mrad by using an illumination-limiting aperture. The EELS spectrum imaging was done using a 0.5 eV or 1 eV energy channel width for an energy range containing 2048 channels. The FWHM of the zero-loss peak was measured as 1.5 eV. EELS elemental distribution and compositional maps were generated using a model-based (Hartree-Slater or Hydrogenic White Lines) quantification routine (excluding ELNES).

X-ray photoelectron spectroscopy (XPS) was performed on a Thermo Scientific ESCALAB 250 Xi spectrometer operating with a monochromatic Al kα (1486.7 eV) source, an X-ray power of 300 W, an X-ray spot size of 900 μm and operating at a pressure of 10^{-8} mBar. Thermogravimetric analysis (TGA) was performed on a PerkinElmer STA6000 analyzer. Nitrogen physisorption experiments were conducted using a Micromeritics Tristar 3000 surface area and porosity analyzer set at – 195 °C, with sample degassing conducted at 150 °C overnight.

Powder X-ray diffraction (PXRD) and Extended X-ray absorption Fine Structure (EXAFS) data were collected at the Canadian Light Source Brockhouse low energy diffraction beamlines and BioXAS spectroscopy beamlines, respectively. Rietveld refinements were performed using TOPAS v7 [10]. Powder diffraction was measured at the Brockhouse lower energy wiggler beamline at the Canadian Light Source, with an incident energy of 15.1 keV, with samples loaded in capillaries that were spinning during the measurements for improved statistics and a Mythen 1K linear detector in the Huber diffractometer 2theta arm. The different snapshots from the detector to cover 2theta range from 10 to 80° were merged into one single PXRD pattern for each sample measurement using a Python routine [11].

2.4. Rietveld refinements

Structure refinements to the diffraction data measured at the CLS

(Brockhouse lower energy diffraction beamline) were performed using TOPAS academic v7 [10]. The instrumental profile was determined by refinement to the measurement of a NIST 660b LaB_6 standard sample. Then, multiphase refinements were performed for the other samples wherein the lattice parameters by symmetry, an isotropic atomic displacement parameter, and scale factor were refined for distinct phases. Peak broadening due to domain size was accounted for by Gaussian and Lorentzian convolutions, and the strain was modelled using the Stephens model for cubic or hexagonal structures. The background was modelled using Chebychev polynomials with 6–8 terms.

2.5. *Pair distribution function analysis*

The high-*Q* total scattering data were collected in capillary transmission geometry at the European Synchrotron Radiation Facility (ESRF) ID11 experimental hutch 1 with a 2D Frelon camera and incident wavelength of 0.1653 Å. The energy calibration was performed on Ni and CeO_2 reference material at seven different sample-to-detector distances. Samples were loaded into Kapton capillaries. The total scattering data were background subtracted, normalized, and Fourier transformed to the pair distribution function (PDF) using the software PDFgetX3 within xPDFsuite [12,13], and structure refinements were performed using PDFgui [14]. Additional total scattering methodology is provided in the supplementary information.

2.6. *X-ray absorption fine structure (EXAFS)*

The Demeter software package [15] was used for data analysis, with Athena and Artemis being the tools of choice. For every merged spectrum, pre- and post-edge backgrounds were subtracted, and the highest point of the first derivative was chosen as Eo. FEFF was used to calculate scattering paths in the EXAFS fitting based on the crystal structure of metallic Ni and metallic Co, NiO, and CoO (fm3m structure). The So2 value was determined by fitting the EXAFS of Co or Ni foil at the same beamline. For the EXAFS fitting of all samples, ΔEo and σ2 were set as identical for all paths and fitted freely. The coordination number (CN) and radial distance I for single and multiple paths were correlated and fitted, as shown in the table provided in the supplementary information (SI4). For Ni edge, EXAFS was fitted at k = 2.5–14 Å-1 and R = 1–4.3 Å and for Co-edge at k = 1.5–12 and R = 1–4.2 Å.

2.7. *Computational method*

The calculations were performed using the first-principles density functional theory (DFT), plane wave pseudopotential method as implemented in the CASTEP module of Materials Studio 2020 [16]. The interaction between the ion and electron is described by the projector-augmented wave method [17]. The exchange and correlation function used in this work is Perdew–Burke Ernzerhof GGA-PBE. The cutoff energy of 400 eV for CoO, 450 eV for NiO and 500 eV for NiCoO. The Brillouin zone integrations are carried out using Monkhorst–Pack K-point mesh [18] with a grid size of 4 × 4 × 4 for total energy calculation. The cobalt 3d74s2, the nickel 3d84s2, and the oxygen 2s22p4 orbitals are treated as valence electrons. The convergence thresholds of 2 × 10-5 eV/atom for the total energy, 0.03 eV/Å for the maximum force, 0.05 Gpa for maximum stress, and 1 × 10-3 Å for the maximum displacements were used to optimize the geometry of crystal structure.

2.8. *Electrochemical measurements*

Catalysts were analyzed using a three-electrode electrochemical cell in a solution of Argon-saturated KOH (1.0 M). A glassy carbon working electrode with a working surface area of 0.196 cm^2 was used in combination with a high surface area graphite rod counter electrode. An Ag/AgCl reference electrode filled with 3.0 M KCl was used. A bridge tube was used as a salt bridge to prevent direct contact between the reference electrode filling solution (3.0 M KCl) and the working electrolyte (1.0 M KOH). Catalyst inks were prepared by mixing 3 mg of the catalyst with 1.5 mL of ultrapure water (18.2 MΩ cm), 1.0 mL of isopropyl alcohol (HPLC grade), and 50 μL of Nafion perfluorinated resin solution (5 wt %) in a mixture of lower aliphatic alcohols and water). The ink was mixed by sonication for 30 min before analysis. The ink (10 μL) was pipetted onto the working area of the working electrode (WE) and dried under rotation at 250 rpm to form a thin film of catalyst. A Biologic SP300 potentiostat and a Biologic Bluerev rotating disk electrode were used for controlling the electrochemical experiments.

In cyclic voltammetry (CV) experiments, the WE were cycled between −0.5 and 0.6 V vs. Ag. AgCl using a scan rate of 50 mV s^{-1} for 50 cycles in an argon-saturated electrolyte until a reproducible CV was obtained. For hydrogen evolution reaction (HER) experiments, the linear sweep voltammetry (LSV) experiments were employed, and the Wes were polarized between −1.5 and 0.5 V vs. Ag.AgCl. In oxygen evolution reactions (OER), the WE electrode was polarized between −0.5 and 2.0 V vs. Ag.AgCl. Both OER and HER were carried out in argon-saturated KOH, using a polarization rate of 5 mV s^{-1} and a continuously rotating disk electrode (RDE) rotation of 1600 rpm. The OER and HER durability studies were investigated using chronoamperometry and LSV. For HER, the WE were polarized at the HER overpotential at 10 mA cm^{-2}, for about 17 h, under 1600 rpm rotation (to continuously remove bubbles of hydrogen or oxygen formed on the WE surface and prevent the catalyst layer from flacking off). For the OER, the same procedure was repeated at an OER overpotential at 10 mA cm^{-2}. Electrochemical impedance spectroscopy was measured for both OER and HER at overpotential at 10 mA cm^{-2} scanning between 100 kHz–0.2 MHz. The double-layer capacitance was measured by scanning in the non-faradaic regions of the CV at incremental scan rates between 10 and 40 mV s^{-1}.

2.9. *Gas chromatography analysis of H_2 and O_2*

The rate of formation of hydrogen and oxygen for the HER and OER was evaluated using an electrochemical 2-electrode cell. The cathode and anode were both 1 cm^2 nickel foam decorated with dried $Ni_xCo_{1-x}O$/HCS catalysts. The electrochemical cell was connected online to the Agilent GC-TCD (Gas Chromatography – Thermal Conductivity Detector). A sample of the gas from the 2-electrode cell headspace was continuously analyzed by gas chromatography (Agilent GC 8820) with a thermal conductivity detector to determine the production rate and Faradaic efficiency towards the rate of H_2 and O_2 production. Special gas mixtures with various compositions of the $H_2/O_2/N_2$ balance (Afrox SA) were used for the calibration of the GC.

3. Results and discussion

The TEM image (Fig. 1a and c) confirms the spherical morphology of the HCS supporting the $Ni_xCo_{1-x}O$ nanoparticle catalysts and their uniform distribution over the support – appearing as small dark spots under 5 nm, on the HCS.

The STEM images (Fig. 1b) show the uniform distribution of the smaller $Ni_xCo_{1-x}O$ nanoparticles which are smaller than 5 nm, whereas the STEM in Fig. 1d shows the mixed distribution of the smaller $Ni_xCo_{1-x}O$ oxide nanoparticles mixed with larger metallic (Ni/Co) nanoparticles with sizes larger than 10 nm. The selected area electron diffraction (SAED) data (Fig. 1 e) shows the diffraction rings for the 111, 200, 220, and 311 crystal planes of the $Ni_xCo_{1-x}O$ confirming the nanocrystalline nature of the Ni and Co oxide composite. Compared to the SAED of the monometallic NiO (Figure SI1 and Table SI1 and SI2), an increase in the 111-lattice spacing is observed. This manifestation of the lattice expansion of the Ni (111) plane can be attributed to the chemical and electronic interaction between the Ni, Co, O, and the C of the $Ni_xCo_{1-x}O$/HCS nanoparticles [19]. From the HRTEM image (Fig. 1f) an edge-on view of the oxide and non-oxide nanoparticles can be seen. The

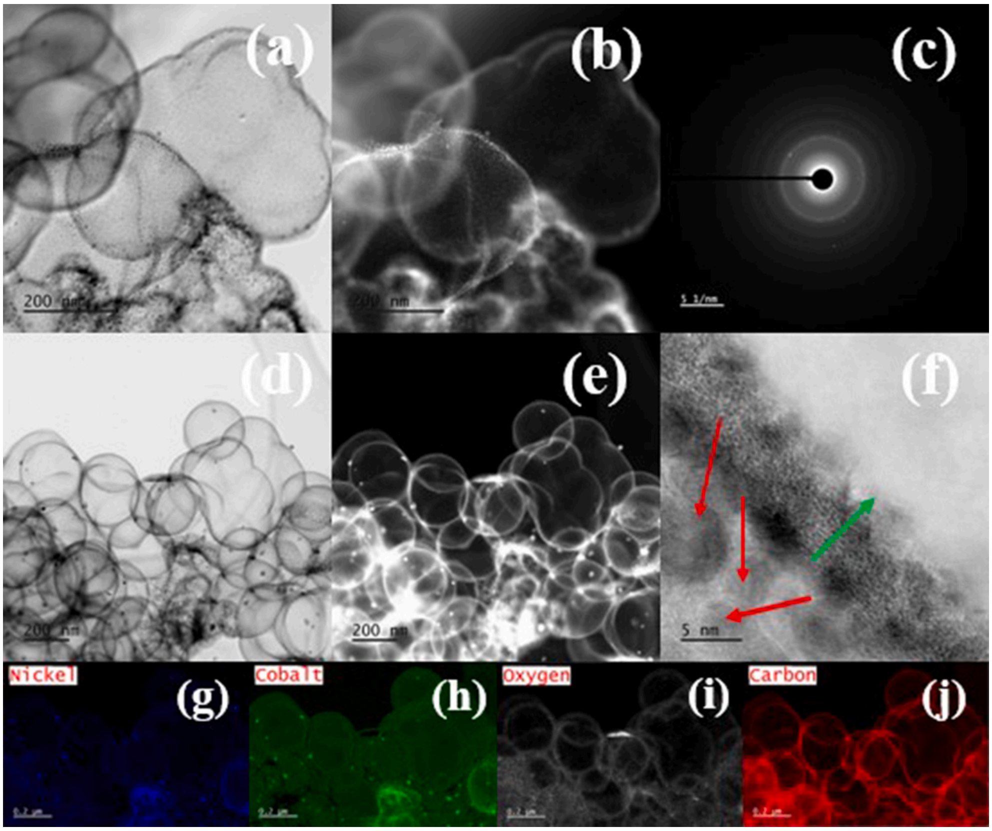

Fig. 1. The $Ni_xCo_{1-x}O$/HCS (a) TEM images of uniform small nanoparticles, (b) STEM image of uniform small nanoparticles) (c) TEM images of a mixture of bimetallic oxide nanoparticles (smaller than 5 nm) and metallic Ni or Co nanoparticle (larger than 10 nm), (d) STEM images of a mixture of bimetallic oxide nanoparticles (smaller than 5 nm) and metallic Ni or Co nanoparticle (brighter spots, larger than 10 nm) small nanoparticles, I SAED of the $Ni_xCo_{1-x}O$/HCS (f) HRTEM showing the graphitic HCS shell (black arrow), the larger crystalline metallic Ni nanoparticle (green arrow), and the $Ni_xCo_{1-x}O$ nanoparticle (red arrow and insert) and, (g–j) elemental maps showing the uniform distribution of the Ni (blue), Co(green), O (light grey) and C (red). (For interpretation of the references to colour in this figure legend, the reader is referred to the Web version of this article.)

metallic particles are encapsulated in a graphitic shell. This is seen everywhere on the catalysts. The smaller oxide particle is showing crystallinity as can be seen from the lattice fringes (Fig. 1f inset). The elemental distribution of the $Ni_xCo_{1-x}O$/HCS catalysts was further elucidated with STEM-EELS for elemental mapping. The electron energy loss (EELS) spectra of the $Ni_xCo_{1-x}O$/HCS (Fig. 1g – j nanoparticles indicate a homogeneous dispersion of Ni, Co, and O that constitutes the $Ni_xCo_{1-x}O$ metal oxide nanoparticles on the HCS support. Such a uniform dispersion is key for the distribution of the electrocatalytic active sites on the surface of the supports.

3.1. *Thermogravimetric analysis, Raman spectroscopy, surface area, and porosity*

The prepared catalysts were analyzed via thermogravimetric analysis (Fig. 2a) to 900 °C in air to facilitate the complete combustion of the catalyst. The mass loss at 100.4 °C is attributed to the evaporation of the atmospheric moisture adsorbed at the surface and inside the pores of the catalyst and HCS support. The mass losses at 308.3 °C and 418.3 °C as shown by the TGA derivative (in red) are attributed to the two different dominant types of carbon present in the HCS respectively. These are the more ordered sp^2 hybridized carbon degrading at a higher temperature (~418 °C) and the less ordered and amorphous carbon degrading at a lower temperature (~308 °C) [20]. Above 500 °C, the final weight of the sample remains at 34 wt% as all the HCS material is combusted with only the $Ni_xCo_{1-x}O$ remaining. The deconvoluted Raman spectra (Fig. 2b) of the catalyst composite confirm the existence of the two primary types of carbon in the HCS in agreement with Raman data, the ordered sp^2 hybridized carbon (G-band) and the sp^3 hybridized diamond-like carbon (D-band) in the sample. The D' and D" bands are attributed to various types of carbon bonded to oxygen present in the catalyst. Usually, these are oxygen-bonded carbons where most of the nucleation of metal nanoparticles occurs during deposition [21].

The textural properties of the materials were investigated using N_2 physisorption. The material demonstrates a type II BET isotherm (Fig. 2c) and a hysteresis loop in the desorption branch ascribed to capillary condensation of the gas molecules due to the meso and microporosity of the materials [22]. These pores are essential for the diffusion of the gaseous products of the HER and OER and the confinement of the metal oxide nanoparticles.

The pore size distribution (Fig. 2d) confirms the pores possess significant volume between 1 and 30 nm, validating the meso and microporosity of the materials. It is in these meso pores and micropores where the bimetallic oxides are deposited inside the pores and on top of pores resulting in significant confinement of the bimetallic oxide nanoparticles. This kind of confinement enhances the electrocatalyst's durability as it prevents the agglomeration and migration of $Ni_xCo_{1-x}O$ nanoparticles [23].

3.2. *X-ray photoelectron spectroscopy*

XPS analysis shows the valence composition of the $Ni_xCo_{1-x}O$/HCS. The XPS survey (Figure SI 2)spectra confirm the existence of C1s, O1s, Ni 2p, and Co 2p peaks at various binding energies. The C1s spectrum (Fig. 3a) was deconvoluted into the contributing C═C, C–C, C═O, O–C═O, and C–O bonds at 284.3, 285.0 eV, 279.1 eV, 288.8 eV, and

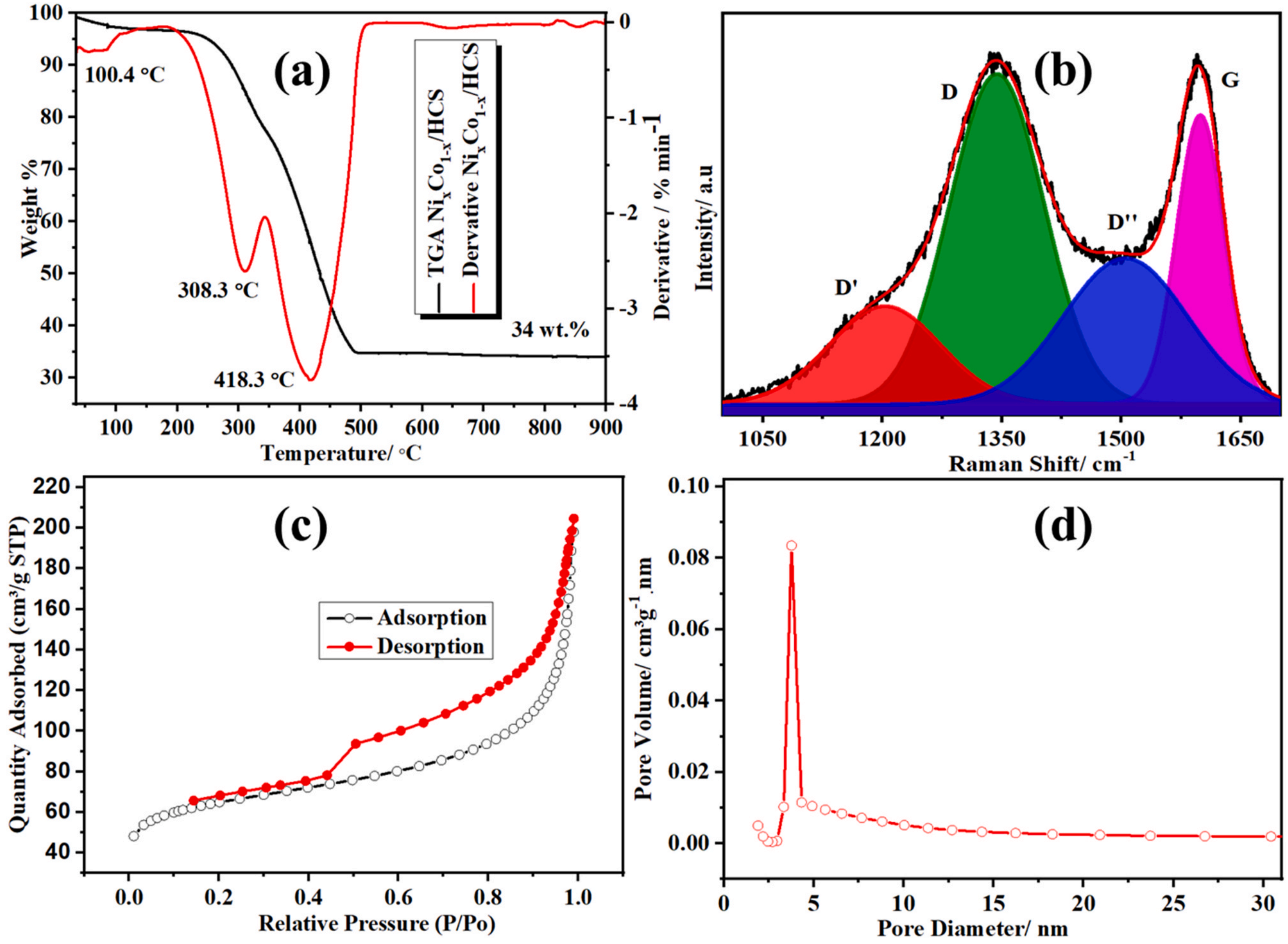

Fig. 2. (a) The TGA plot (b) Raman Spectra, (c) BET isotherm and (d) BET pore size distribution of the of $Ni_xCo_{1-x}O$/HCS catalyst.

286.1 eV in agreement with the TGA and Raman data [24]. The O1s spectrum (Fig. 3b) was deconvoluted into the contributing metal-oxide (529.5 eV), C=O (532.9 eV), and the C–O (531.4 eV) bonds [25].

Both the C1s and O1s demonstrate the existence of a highly functionalized surface of the HCS as well as the existence of both graphitic and amorphous carbon. The amorphous and oxygen-functionalized components of the HCS provide anchoring sites for the metal oxide nanoparticles through chemical and physical bonding [26] with the electron density in the oxygen functional groups promoting a metal oxide nanoparticle nucleation profile that favours the formation of smaller particle domains [27]. The graphitic carbon component is essential for the electrochemical stability and activity of the material in electrochemical processes as the sp^2 bonds in the HCS carbon are much stronger than the sp^3 bonds. The stronger bonds require more energy to break, thereby reducing the electrochemical degradation of the carbon support and enhancing conductivity due to the lone pair of electrons involved in the bonding [28]. The existence of the well-pronounced metal-oxide peak confirms the extensive oxidation of Ni and Co as they exist in the $Ni_xCo_{1-x}O$/HCS. The Ni 2p spectrum (Fig. 3c) was deconvoluted into two coupled Ni $2p_{3/2}$ (855.2 eV) and Ni $2p_{1/2}$ (873.8 eV) corresponding to the dominant Ni^{2+} oxidation state. There is also a small contribution of metallic Ni (853.2 and 871.6 eV). The Co 2p spectrum (Fig. 3d) was deconvoluted and shows a small contribution of metallic cobalt (777.8 and 793.4 eV) with coupled doublets of Co $2p_{3/2}$ (781.5 eV) and Co $2p_{1/2}$ (796.3 eV) [29]. The deconvoluted Ni2p and Co2p spectra do not show the presence of Co^+ and Ni^+ species.

3.3. Powder X-ray diffraction (PXRD) and pair distribution function (PDF) analysis

To determine the phases present in the samples studied herein, high-resolution synchrotron diffraction data were measured at the Canadian light source. To further confirm the phase distribution and investigate the local bonding behavior within the phases, complementary high-energy total scattering measurements were performed at the ESRF. By measuring both Bragg and diffuse scattering over a wide range of momentum transfer, the pair distribution function (PDF) could be reliably determined with a high real-space resolution.

In short, the PDF represents a weighted histogram of atom-pair distances in the material, which provides a measure of the local structure even in the absence of long-range order. This makes it useful for characterizing the structure of small nanoparticles [30], from which highly broadened Bragg diffraction is difficult to analyze directly, and Rietveld refinement reaches its limit. An example is shown in Fig. 4, for a NaCl-type metal oxide structure where peaks associated with the nearest neighbor metal-oxygen (M − O) and M-M/O–O distances can be clearly observed. For the second peak, the O–O part only contributes a small part of the total since the partial contributions are weighted by the number of electrons on the atoms in the corresponding pairs; see the relative scattering power and partial contributions of each pair of atoms in SI Fig. 3. A detailed derivation and further discussion of the PDF is provided in the freely available reference [31].

The diffraction and PDF data for CoO/HCS, NiO/HCS, and $Ni_xCo_{1-x}O_x$/HCS are presented in Fig. 5. We determined the phases present by a combined analysis of all three datasets. The associated fits resulting from multiphase Rietveld refinement or real-space PDF refinement are shown

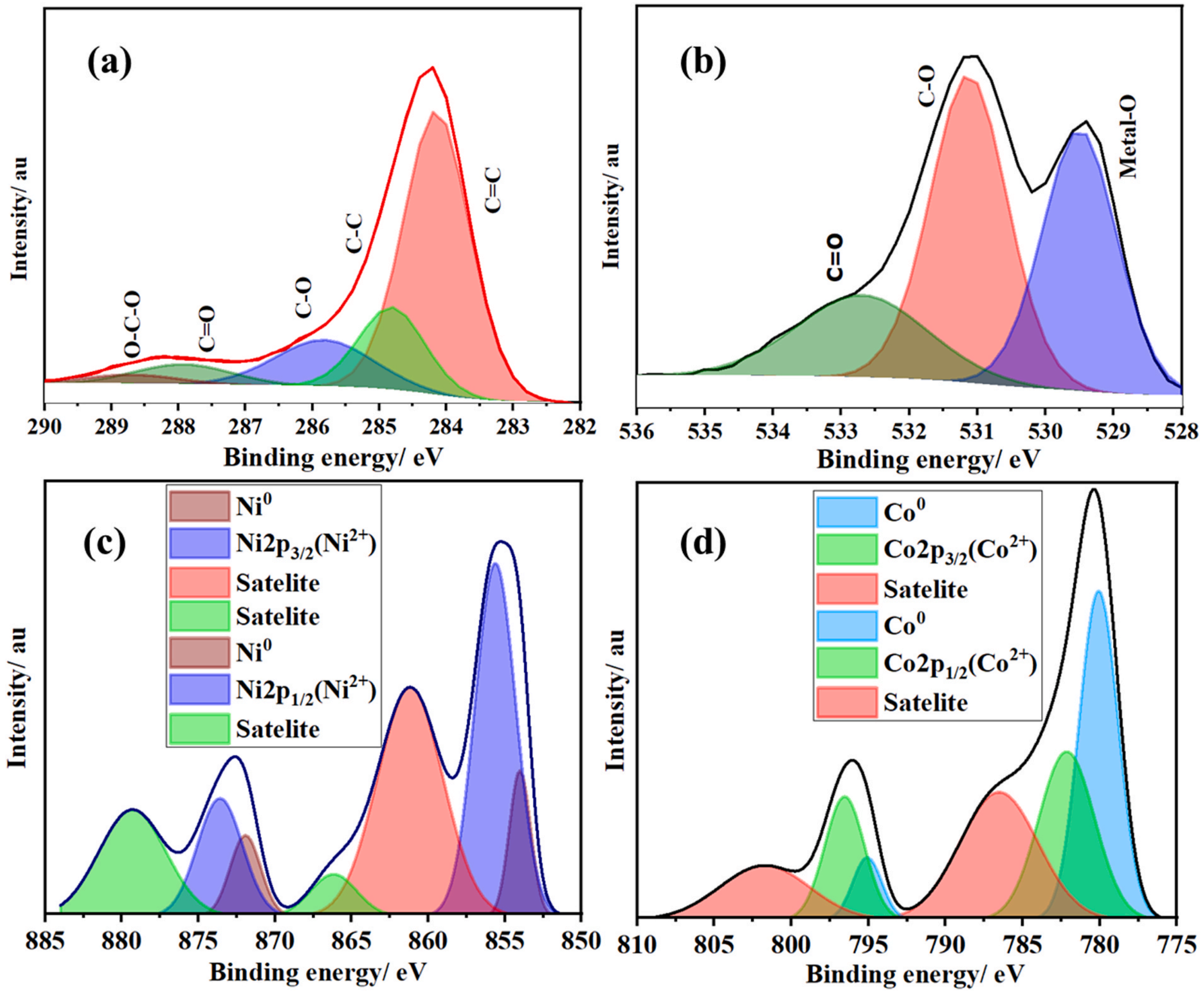

Fig. 3. The deconvoluted X-ray photoelectron spectra of the $Ni_xCo_{1-x}O$/HCS, (a) C1s, (b) O1s, (c) Ni2p, and (d) Co 2p.

for comparison (see SI Fig. 3–12 for further details). $Ni_xCo_{1-x}O$/HCS forms the same phases observed for NiO/HCS, consisting of predominantly NaCl-type metal oxide nanoparticles in the ultra-small diameter range of 1–5 nm and a minority fraction of fcc-type metal nanoparticles with approximately 10 nm diameter. In contrast, CoO/HCS forms a distribution of oxide phases including NaCl-, zincblende-, and wurtzite-type structures. In this case, there is a higher uncertainty in the quantification of NaCl-type and wurtzite-type phases between Rietveld and PDF refinements. This might be due to a large fraction of nearly amorphous wurtzite-type phase observed in the PDF (not easily detected in the diffraction pattern) or speculatively by the presence of stacking faults hinted at by somewhat triangular-shaped peaks and slight misfit of some low-order diffraction peaks. We could not detect any peaks associated with pure cobalt/nickel metal in the diffraction pattern, although a small peak associated with an atom-pair distance of Å. 2.5 Å in the PDF could be tentatively assigned to the presence of a very small cobalt metal content at the level of a couple of weight percent. Cases where multiple of the same phase were used to better approximate the size distribution likely indicate a lognormal distribution of domain sizes, but this was not further investigated.

[a]Structure type: NaCl (PDF card – 01-076-3832, ICSD-9865); [b]Structure type: wurtzite (PDF card – 04-005-9659); [c]Structure type: zinc blende (ICSD-29082); [d]Structure type: fcc; [e]Structure type: NaCl; [f]Structure type: fcc; [g]In some cases, two separate phases were used to describe a structure if distinct crystallite size distributions were distinguished. [e]Crystallite domain sizes estimated from Rietveld refinement using the volume-weighted mean column lengths determined from the integral breadth Lvol-IB. [f]Crystallite domain sizes estimated from PDF refinement using damping parameters based on spherical domain function (see Table 1).

Due to the one-electron difference between Ni and Co, we cannot distinguish separate contributions between the two elements by scattering power or bond length and must treat them in an aggregate fashion. The composition of the phases used to model the $Ni_xCo_{1-x}O$/HCS sample was approximated by fixing at $Ni_{0.5}Co_{0.5}$. We investigated the distances associated with the nearest neighbor (metal-oxygen) M − O and (metal-metal) M-M pairs using the refined structure models and structure-independent peak fitting using Gaussian peaks, shown in Table 2. For CoO/HCS, we obtained very consistent results between the two methods indicating a good match of the bond distances to the bulk phases identified. For both NiO/HCS and $Ni_xCo_{1-x}O$/HCS, we observe a misfit of the M − O peak from the fit of the structure models, see insets in Fig. 5(e and h). Peak fitting confirms a shift to slightly shorter distances in the experimental data. With a large fraction of metal oxide NPs on the order of 1–2 nm, there may be an average contraction of M − O bond distances associated with high surface strains, although this may be counter to typically observed lattice expansion for decreasing size in metal-oxide nanoparticles [32]. On the other hand, Ni–C distances are approximately 1.87 Å for the experimentally observed Ni_3C structure (ICSD-17005, MP-7586) [33] and expected to be 2.03 Å for NaCl-type NiC (MP-1009582). Therefore, it is also plausible that the shifting could result from some carbon incorporation into the NiO structure. For $Ni_xCo_{1-x}O$/HCS, the M − O peak is slightly broadened, and the M-M peak slightly shifted to higher distances relative to NiO/HCS, SI Fig. 11. The

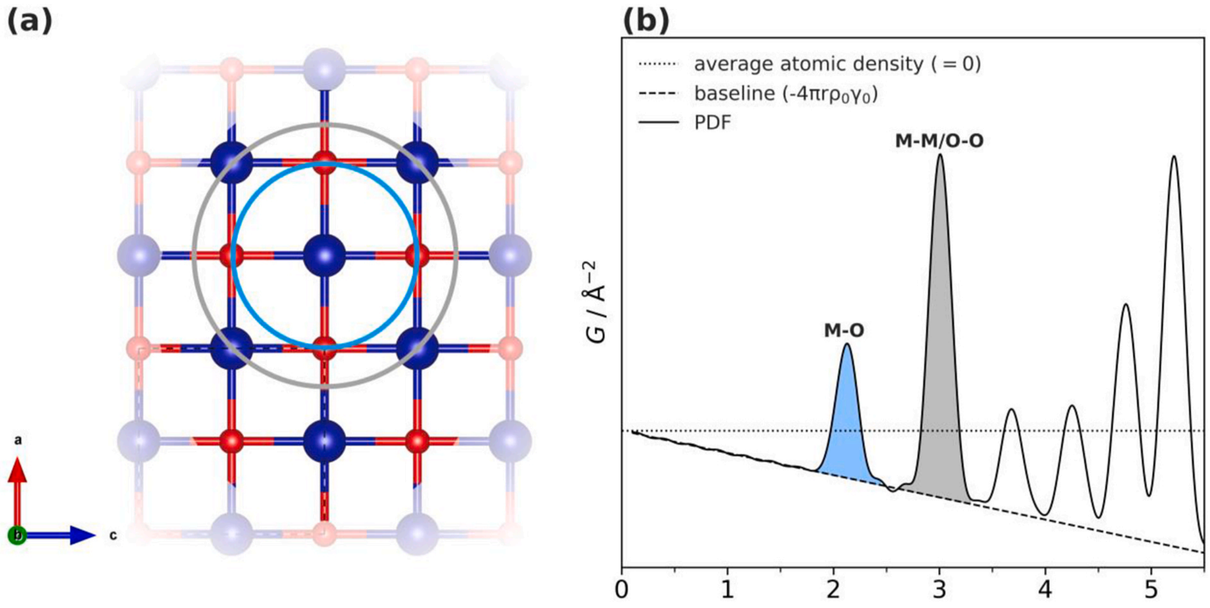

Fig. 4. An example of the pair distribution function for assessment of atomic-pair distances (a) A slice of NaCl-type structure (e.g. NiO). is shown as viewed along the [010] direction with metal atoms in blue and oxygen in red. Concentric circles around a metal atom show slices of the nearest neighbor metal-oxygen (M − O) and metal-metal (M–M) coordination spheres. (b) The pair distribution function (PDF) as simulated for the given structure is shown, with the first two peaks corresponding to the coordination distances in (a). (For interpretation of the references to colour in this figure legend, the reader is referred to the Web version of this article.)

former suggests some short-range disorder in the M − O distance distribution due to the mixture of Co and Ni in the NiO structure, while the increased M-M distance suggests a slight structural expansion due to the presence of slightly bigger Co ions.

[a]The Co–Co distance should be longer than Ni–Ni, but the observed distance is less certain due to its relatively low intensity. [b]Pair-distances averaged between two same-structure phases in the model. [c]Separate contributions to the Co–O peak cannot be resolved directly. [d]Peaks observable by structure-independent fitting were assigned to their primary contributions based on comparison to the most similar pair distances in the models.

We compared the PDF measured for HCS alone to the residual signals of the sample PDFs (processed without subtracting the support scattering background) minus the simulated contributions from the refined phases (SI Figure 12). In this case, residuals represent the structure of the support plus any structural correlations unfit by the bulk phase models. Prominent signals remaining from misfits of the NiO-type phase are present for NiO/HCS and $Ni_xCo_{1\text{-}x}O$/HCS, whereas the residual is more like the HCS support for CoO/HCS. As noted above, misfits in the local correlations of the NiO-type phases in the former two cases may be due to structural effects resulting from the ultrasmall size of the particles. They may imply some increased interaction of carbon with the nanoparticles or from local structural distortions not accounted for in the long-range model.

3.4. *Extended X-ray absorption fine structure (EXAFS)*

The magnitudes of the Fourier-transformed (FT) extended X-ray absorption fine structure (EXAFS) signals acquired at the Nickel (Ni) and Cobalt (Co) K-edges for NiO/HCS, CoO/HCS, and $Ni_xCo_{1\text{-}x}O$/HCS are shown in Fig. 6. Within the Radial ® space, the FT K3-weighted EXAFS spectra of $Ni_xCo_{1\text{-}x}O$/HCS at the Ni K-edge reveal peaks at 1.70, 2.20, and 2.60 Å, which correspond to the Ni–O and Ni–Ni coordination to Co (Ni–Ni/Co) and O (Ni–Ni/O) atoms, respectively [34]. Similarly, the FT K3-weighted EXAFS spectra at the Co K-edge for $Ni_xCo_{1\text{-}x}O$/HCS exhibit peaks at 1.50, 2.20, and 2.50 Å, signifying the Co–O and Co–Co coordination to Ni and O, respectively [35]. This observation confirms the presence of Ni^0, Co^0, Ni^{2+}, and Co^{2+} species within the sample. The shifts towards higher radial distances for the Ni–O and Co–O bonds from 1.50 to 1.70 Å, when compared to the monometallic NiO/HCS and CoO/HCS standards, are attributed to alterations in the electronic structure due to the interaction/coordination between NiO and Co in the $Ni_xCo_{1\text{-}x}O$/HCS catalyst [34,35]. This phenomenon is likely due to some degree of Co incorporation into the Ni–O structure, leading to an expansion of the Ni–O bonds, as alluded to, by the PDF fits. The significant disparities in the Fourier-transformed K3-weighted EXAFS spectra of $Ni_xCo_{1\text{-}x}O$/HCS, in contrast to NiO/HCS and CoO/HCS, are derived from electronic modulation and coupling arising from the interaction between Co and NiO in the former, which is absent in both later due to their monometallic nature [36]. These distinctions in the spectra are indicative of unique coordination environments for Ni and Co in $Ni_xCo_{1\text{-}x}O$/HCS as compared to the monometallic NiO/HCS and CoO/HCS catalysts.

The Ni and Co K-edge K3χ (k) oscillation curves depicted in Fig. 6c-d for $Ni_xCo_{1\text{-}x}O$/HCS demonstrate varying amplitudes of k values when compared to NiO/HCS and CoO/HCS samples, also, suggesting dissimilar coordination environments within these catalysts [37]. Notably, the fitted coordination number for the nearest neighboring Ni–O bond in the first coordination shell in the $Ni_xCo_{1\text{-}x}O$/HCS sample is 5.5 (Table SI 3), which is slightly lower than the observed value of 6.5 for NiO/HCS. This minor reduction in coordination number for Ni in the bimetallic $Ni_xCo_{1\text{-}x}O$/HCS composite is attributed to structural distortion in the Ni–O lattice due to Co incorporation [38]. Additionally, the lower Debye-Waller factor of 0.008 (Table SI 3) in NiO/HCS, in contrast to 0.01 for the bimetallic composite, suggests that Ni and O atoms are more favorably bonded in NiO/HCS than in $Ni_xCo_{1\text{-}x}O$/HCS, owing to the influence of Co doping in the bimetallic composite's structure [39]. These variations in the Debye-Waller factor are ascribed to differences in local structural disorder within crystalline domains, the nanomaterial environment.

3.5. *Electrochemical activity*

The HER activity of the $Ni_xCo_{1\text{-}x}O$/HCS composites was investigated

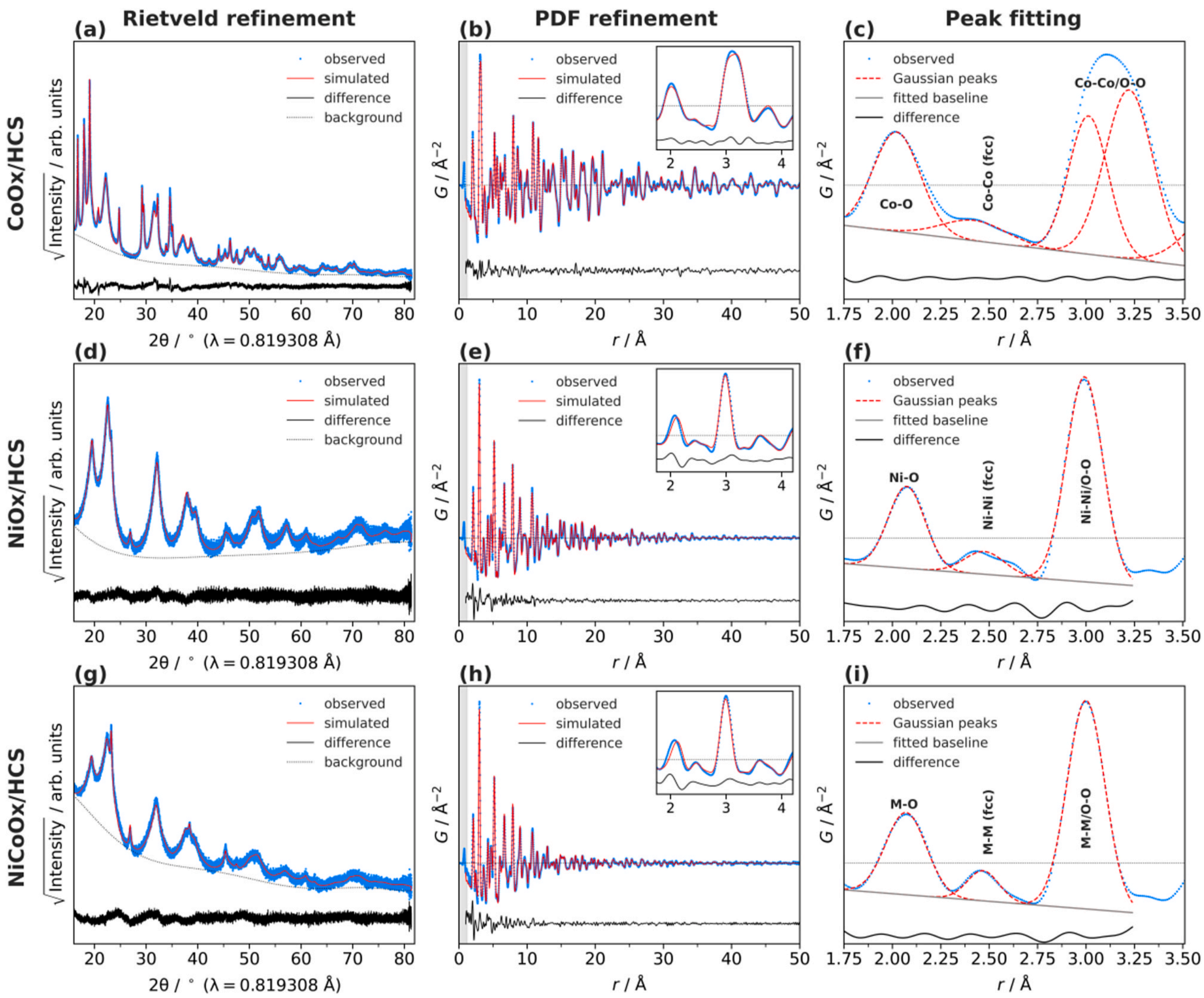

Fig. 5. The high-resolution diffraction patterns and resulting pattern from Rietveld refinement, pair distribution function (PDF) with resulting PDF from real-space refinement, and results of structure-independent peak fitting to the first few atom-pair coordination shells in the local structure are shown for (a-b-c) CoO/HCS, (d-e-f) NiO/HCS, and (g-h-i) $Ni_xCo_{1-x}O$/HCS. The horizontal lines in the PDF subplots represent $G(r) = 0$, with the difference curves offset below. HCS support was subtracted as part of the background for the refinements shown here.

Table 1
Overview of the phase fractions and crystallite domain sizes (D_c) determined by structure refinements to the high-resolution PXRD and high-energy total scattering PDF data.

Sample	Phase	Rietveld refinement[g]		PDF refinement[g]	
		wt%	D_c/nm[e]	wt%	D_c/nm[f]
CoO/HCS	CoO (*Fm-3m*)[a]	59	3	38 { 20 18	2 6
	CoO (*P6₃mc*)[b]	28	40	50 { 24 26	– 1
	CoO (*F-43m*)[c]	13	27	10	15
	Co (*Fm-3m*)[d]	–	–	2	2
NiO/HCS	NiO (*Fm-3m*)[e]	97 { 72 25	2 4	96 { 70 26	1 5
	Ni (*Fm-3m*)[f]	3	12	4	10
$Ni_xCo_{1-x}O$/HCS	NiCoO (*Fm-3m*)[e]	93 { 76 17	2 5	96 { 75 21	1 3
	NiCo (*Fm-3m*)[f]	7	14	4	10

Table 2
Overview of the local atom-pair distances determined from the PDF data.

Sample	Phase	Pair-distances			
		Structure refinement		Peak fitting	
		M-O	M-M	M-O	M-M
CoO/HCS	CoO (*Fm-3m*)	2.13	3.02	2.03[c]	3.02[d]
	CoO (*P6₃mc*)	1.97	3.22		3.23[d]
	CoO (*F-43m*)	1.96, 2.03	3.21, 3.25		
	Co (*Fm-3m*)	–	2.43[a]	–	2.43
NiO/HCS	NiO (*Fm-3m*)	2.11[b]	2.98[b]	2.08	3.00
	Ni (*Fm-3m*)	–	2.50	–	2.48
$Ni_xCo_{1-x}O$/HCS	NiCoO (*Fm-3m*)	2.12[b]	2.99[b]	2.08	3.00
	NiCo (*Fm-3m*)	–	2.50	–	2.47

using electrochemical measurements in a 3-electrode cell setup and 1.0 M KOH electrolyte. All the electrochemical data was compensated for solution resistance and the Ag. AgCl reference electrode potentials were converted to the standard reversible hydrogen electrode (RHE), using equation (1).

$E\ (RHE) = Eag/AgCl + 0.059\ pH + E^{o}Ag/AgCl.$ (1) [40]

Where $E^{o}Ag/AgCl = 0.1976$ V at 25 °C and E Ag/AgCl is the measured WE potential and the of the 1.0 M KOH electrolyte.

The HER polarization curves exhibit an earlier onset for the HER

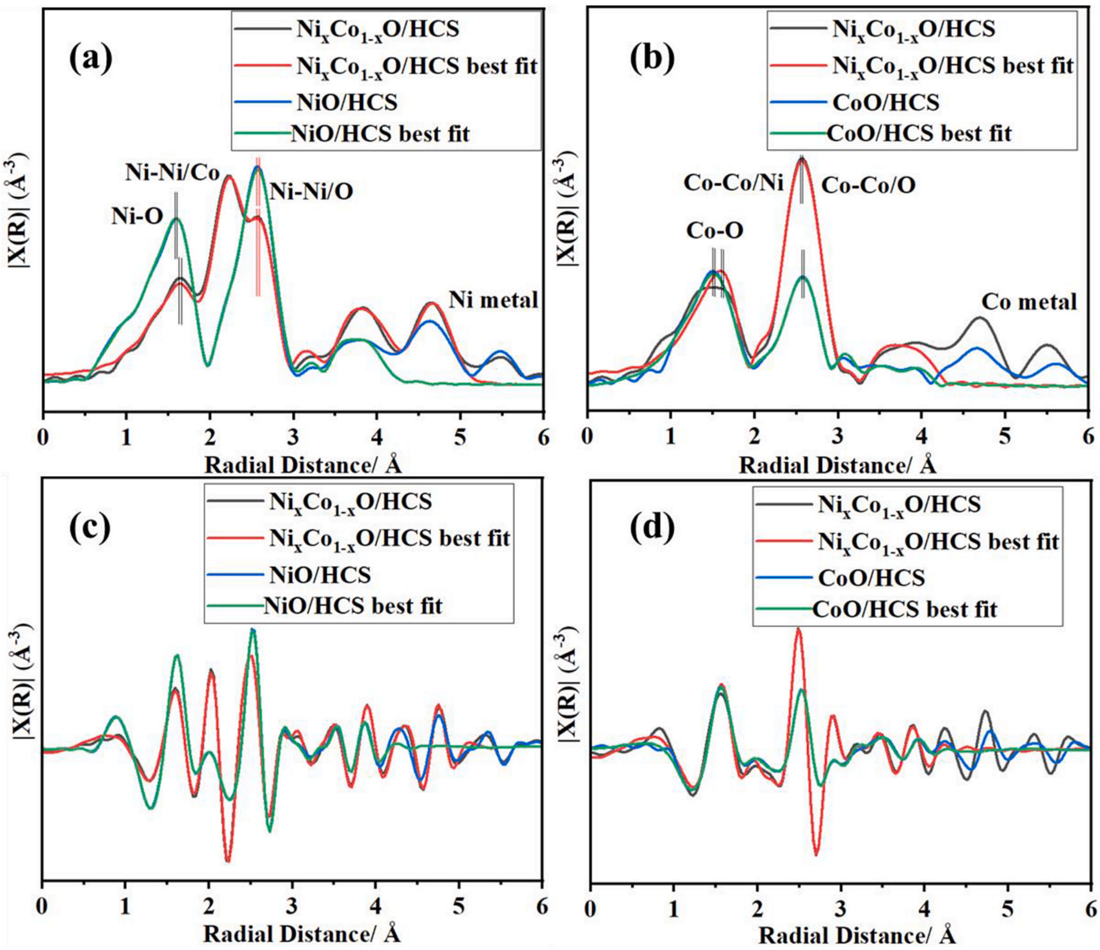

Fig. 6. Fourier-transformed (FT) extended X-ray absorption fine structure (EXAFS) at the Nickel (Ni) (a and c) and Cobalt (Co) (b and d) K-edges of the $Ni_xCo_{1-x}O$/HCS bimetallic oxide and the monometallic NiO/HCS and CoO/HCS.

process for the $Ni_xCo_{1-x}O$/HCS compared to the monometallic NiO/HCS and CoO/HCS (Fig. 7a). At the current density of 10 mAcm^{-2}, the bimetallic composite exhibits an HER overpotential of 178.6 mV compared to 305.3 mV and 315.8 mV for the NiO/HCS and CoO/HCS respectively.

The LSV polarization curves were fitted to the Tafel equation, $\eta = b \log j + a$ (2) [40].

Where j is the current density, b is the Tafel slope, and a is the intercept. A lower Tafel slope of 68.2 ± 5 mVdec^{-1} was observed for the $Ni_xCo_{1-x}O$/HCS compared to the NiO/HCS (108.4 ± 2 mVdec^{-1}) and the CoO/HCS (112.7 ± 9 mVdec^{-1}), (Fig. 7b), demonstrating faster reaction kinetics and a favourable reaction mechanism towards the HER process. As the Tafel slope for the bimetallic $Ni_xCo_{1-x}O$/HCS composite is between 30 and 120 mVdec^{-1}, this is attributed to an HER reaction mechanism that is slower than the chemical reaction Tafel mechanism (equation (3)) but faster than the electrochemical Heyrovsky mechanism (equation (4)).

$$2M - H_{ads} \rightleftharpoons 2M + H_2 \tag{3}$$

(Tafel reaction – Tafel slope lower than 30 mVdec^{-1})

$$H_2O + M - H_{ads} + e - \ \rightleftharpoons M + H_2 + OH^- \tag{4}$$

(Heyrovsky reaction – Tafel slope lower than 120 mVdeC^{-1})

$H_2O + M + e \rightleftharpoons M\text{-}H_{ads} + OH^-$ (5) [41]

(Volmer reaction -Tafel Slope lower than 40 mVdeC^{-1})

Moreover, the $Ni_xCo_{1-x}O$/HCS further demonstrates better reaction kinetics and favourable electro-catalytic mechanism towards HER through a higher exchange current density of 0.615 mAcm^{-2} compared to that of CoO/HCS (0.094 mAcm^{-2}) and NiO/HCS (0.113 mAcm^{-2}). The HER electrochemical impedance spectra were fitted to an equivalence circuit (Fig. 7c) and a low charge transfer resistance of 14 Ω was deduced, compared to 27 Ω and 43 Ω for the NiO/HCS and CoO/HCS respectively. The low charge transfer resistance of the bimetallic catalysts is attributed to a heterostructure and enhanced surface properties of the bimetallic catalyst due to the compositing effect between the Ni and Co oxides [42–44] The inductive behaviour at lower frequencies and higher overpotential agrees with the observed Tafel slope of 68.2 ± 5 mV.dec^{-1}. The inductive behaviour demonstrates that the HER mechanism cannot follow the direct and fastest kinetics Tafel mechanism alone [45]. The HER data for the bimetallic composite is indicative of a mixed Volmer-Heyrovsky mechanism (equations 4 and 5) whereby firstly a molecule of hydrogen is adsorbed(H-ads) on a $Ni_xCo_{1-x}O$ active site (Volmer process) followed by the electrochemical combination of two adsorbed molecules of H_2 (H-ads + H-ads + $Ni_xCo_{1-x}O$) and desorption of H_2 gas (Heyrovsky process). After polarization at the HER overpotential, the current density of the process did not decrease, instead, the overpotential to achieve 10 mA cm^{-2} for the HER became smaller (Fig. 7d) indicating the occurrence of a process on the surface of the electrocatalysts that exposes and maintains the critical active HER sites on the $Ni_xCo_{1-x}O$/HCS composites [46].

The OER polarization curves of the $Ni_xCo_{1-x}O$/HCS (Fig. 8a)

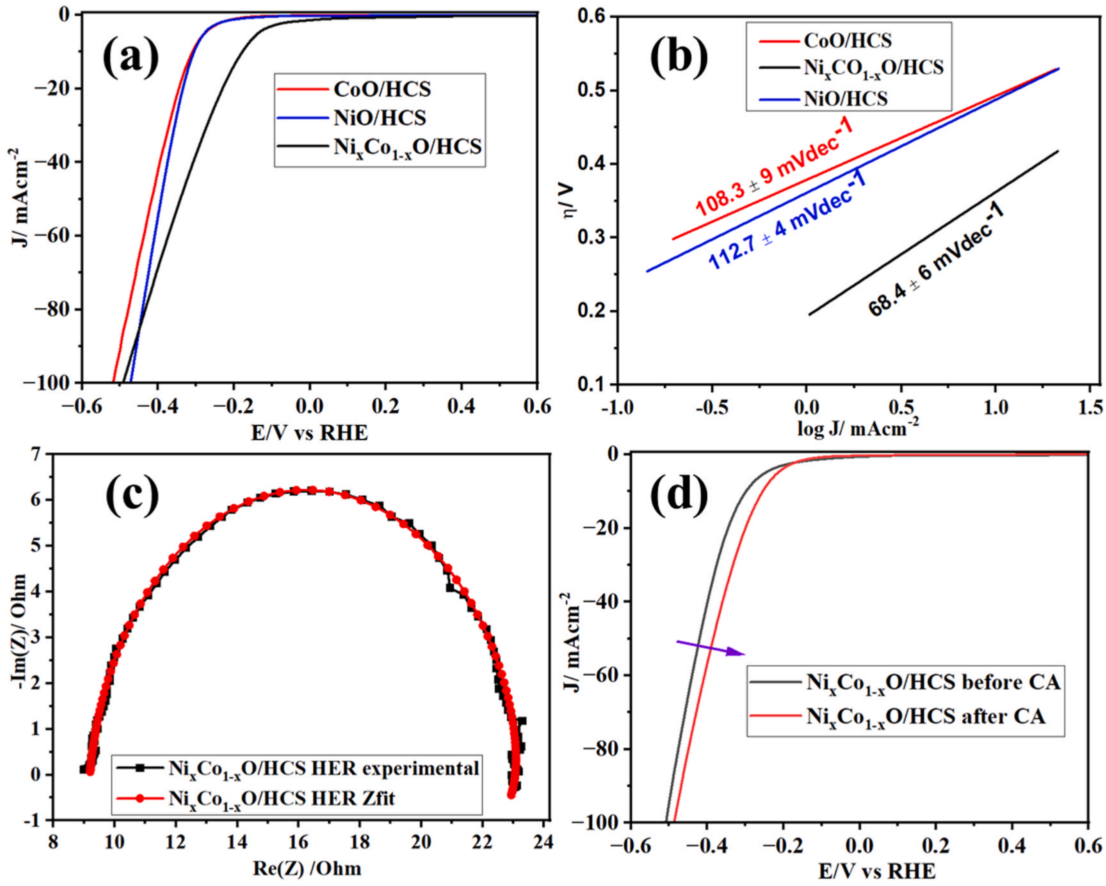

Fig. 7. The HER data for the Ni$_x$Co$_{1-x}$O/HCS, NiO/HCS, and CoO/HCS (a) LSV polarization curves and (b) Tafel slopes. (c) The EIS z-fit of the CoNiO/HCS and (d) the LSV polarization curves before and after 21 h of chronoamperometry.

demonstrate an earlier onset potential compared to the monometallic NiO/HCS and CoO/HCS catalysts. An overpotential of 276.4 mV for the OER process was observed coupled with a small Tafel slope of 52.1 ± 3 mV.dec^{-1} (Fig. 8b), an exchange current density of 0.886 mA cm^{-2} and a charge transfer resistance of 10 Ω, demonstrating faster and more favourable kinetics toward the OER process. The reduction in the Tafel slope of the Ni$_x$Co$_{1-x}$O/HCS compared to the monometallic CoO/HCS (74.3 ± 8 mVdec^{-1}) and NiO/HCS (68.1 ± 5 mVdec^{-1}) indicates a beneficial synergy between the two metal oxides which favours kinetically feasible OER [34]. The EIS spectra of the Ni$_x$Co$_{1-x}$O/HCS were fitted using the equivalence circuit shown (Fig. 8c) and a charge transfer resistance (R_{ct}) of 10 Ω was obtained, which was smaller than those observed for the CoO/HCS (44 Ω) and the NiO/HCS (39 Ω). The stability of the catalysts was also investigated using chronoamperometry (Fig. 9a). The Ni$_x$Co$_{1-x}$O/HCS catalysts were polarized at both the HER (178.6 mV) and OER (276.4 mV) overpotentials for over 17 h and as observed, the current density initially increased (OER) due to the high surface area of the smaller than 2 nm bimetallic oxide crystallites providing abundant active sites for electrocatalysis. In the second hour of CA, a sharp decline in stability could be attributed to the fast agglomeration of the smaller bimetallic oxide crystallites during the water splitting. However, there was a marked increase in the current density after the initial 3 h (Fig. 7a) possibly due to electronic modification of the Ni–O by the presence of the Co–O as CA cycling occurred. The long-term stability over 17 h could be due to the formation of an active and stable catalyst phase formed in situ, or the significant exposure of the pore-confined Ni$_x$Co$_{1-x}$O/HCS catalytic active sites as small portions of the C support were electrochemically degraded, as the electrocatalytic reaction progressed. Similarly, the CA for HER demonstrate significant stability, with minimal decline in the cell current density [47].

After 17 h of CA, the overpotential for the OER decreased to 270 mV due to possibly the exposure of more of the catalyst's activate sites due to some carbon degradation. The observed catalytic trends in OER and HER are correlated to the calculated double-layer capacitance (C_{dl}) (Fig. 9b) of the Ni$_x$Co$_{1-x}$O/HCS catalyst of 35.3 mF cm^{-2} which is significantly higher than for the monometallic CoO/HCS (2.3 mF cm^{-2}) and NiO/HCS (13.6 mF cm^{-2}).

As the C_{dl} is proportional to the electrochemically active surface area (ECSA), the obtained enhanced activity alludes to a plethora of catalytic active sites on the Ni$_x$Co$_{1-x}$O/HCS exposed for the electro-catalytic process [48]. The summary of the electrochemical OER and HER data is provided in Fig. 10.

In addition, the Ni$_x$Co$_{1-x}$O/HCS catalyst outperformed a significant number of previously reported transition metal-based HER and OER catalysts in 1.0 M KOH electrolyte (Table SI5) [8,49,50,51,52,53,54,55].

The enhanced activity and stability toward HER and OER are related to the observed smaller domain size of 1–5 nm as confirmed by PDF and TEM measurements of the bimetallic oxide composite and the strong bimetallic oxide-support anchoring. As smaller nanoparticle domains possess high surface energy, they facilitate faster electron transfer compared to larger thermodynamically stable nanoparticles [56]. Also, the PDF refined M − O and M-M bond distances in the Ni$_x$Co$_{1-x}$O/HCS composite show slight elongation compared to the monometallic NiO and CoO composites. As visually observed in the PDFs and the PDF refinement, the slight expansion of the M − O and M-M bond distances in the bimetallic composite might be associated with high surface strain in the crystal structure of the catalysts which indicates significant promotion of a thermodynamically and kinetically favourable profile for the adsorption of the hydrogen (H-ads), and oxygen (O-ads)

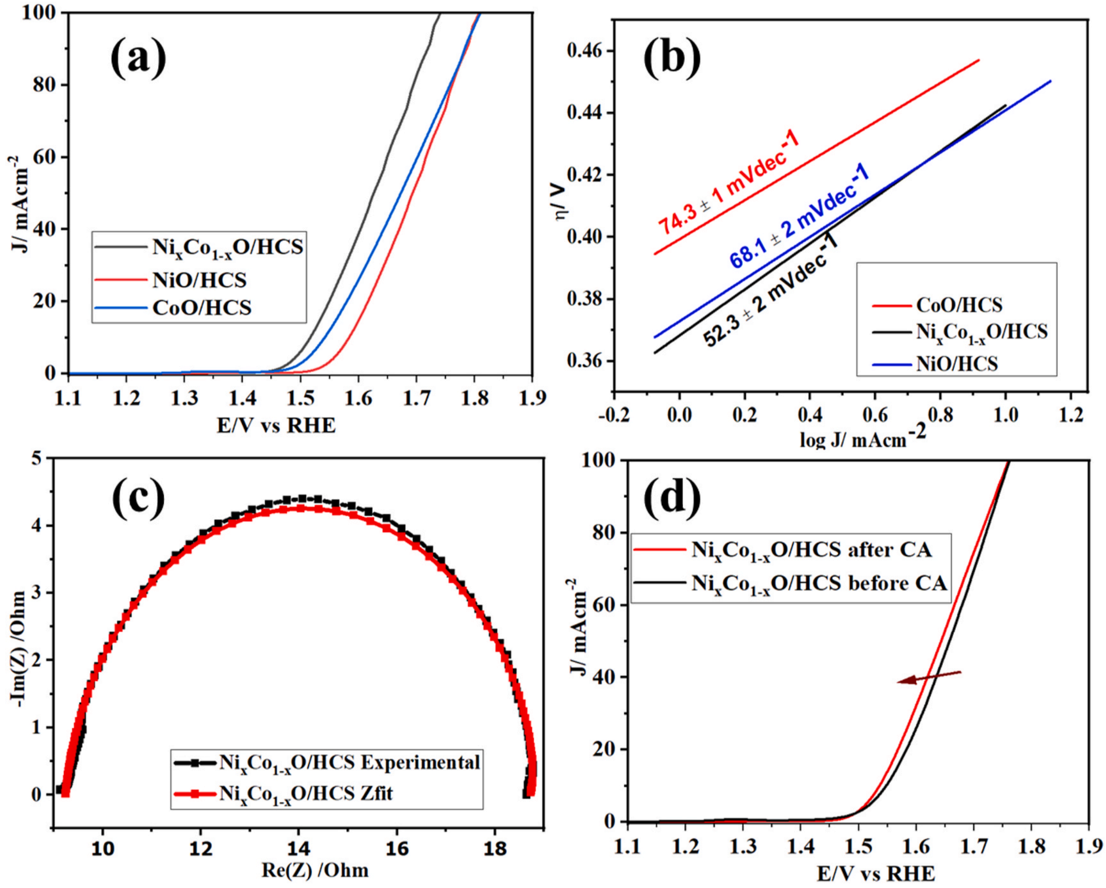

Fig. 8. The OER data for the $Ni_xCo_{1-x}O$/HCS, NiO/HCS and CoO/HCS (a) LSV polarization curves and (b) Tafel slopes. (c) The EIS z-fit of the $NixCo_{1-x}O$/HCS and (d) the LSV polarization curves before and after 21 h of chronoamperometry.

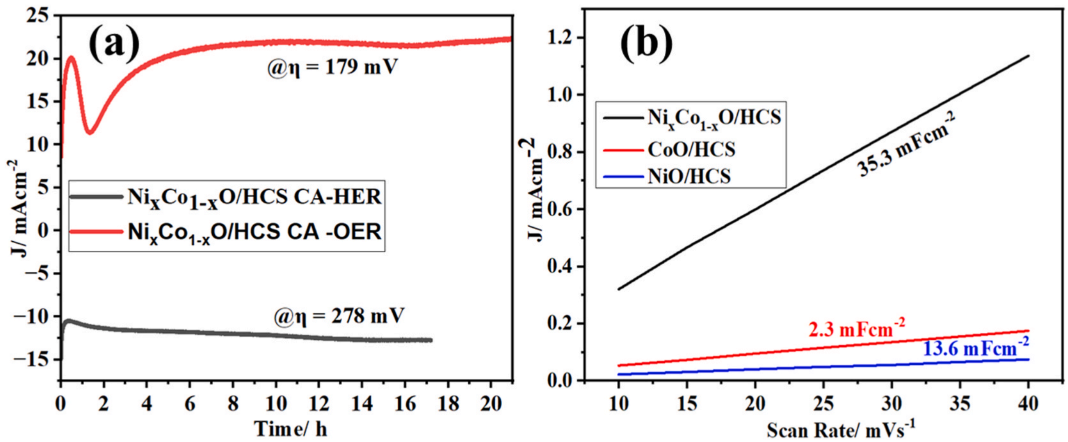

Fig. 9. (a) The HER and OER chronoamperomegrams of the $Ni_xCo_{1-x}O$/HCS and the double layer capacitance (Cdl) of the $Ni_xCo_{1-x}O$/HCS, CoO/HCS and the NiO/HCS.

intermediates and the subsequent desorption of the H_2 and O_2 products. The elongation of the M − O and M-M bonds could be attributed to the C or Co doping into the Ni–O structure. This incorporation of electrochemically active Co into the Ni − O structure reduces the distance electrons must flow between the Ni and the O, thereby enhancing the electronic conductivity and activity of the catalyst [5]. Furthermore, the experimentally observed Ni–C distances of 1.87 Å are shorter than the Ni–C distances for a modelled NaCl type NiC structure demonstrating a shift that is likely because of the carbon doping into the M − O structure. This carbon doping and incorporation of Co atoms into the Ni–O structure would act to enhance the electron flow in the composite facilitating improved electrocatalysis. The PDF fits also indicate the presence of some M-M bonding in the composite. These metallic bonds aid fast electron flow on the surface of the catalyst due to the nature of localized electron density on the surface of the metals. In addition, the stability of the catalysts can also be attributed to the small particle sizes of the bimetallic oxides which are easily confined inside the pores of the HCS support. As the electrochemical process proceeds, these confined nanoparticles remained in contact with the HCS support due to the electronic interaction of the metal oxide with the oxygen groups on the

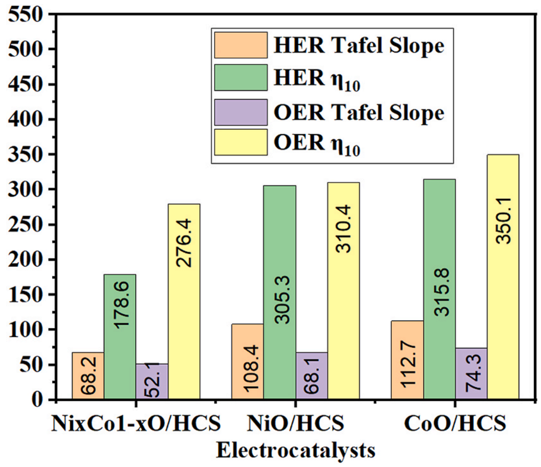

Fig. 10. The summary HER and OER data showing the overpotential and Tafel slopes for the Ni$_x$Co$_{1-x}$O/HCS, CoO/HCS, and NiO/HCS.

surface of the support resulting in strong anchoring of the metal oxides and reduced dissolution of the bimetallic nanoparticles. Moreover, the pore structure restricts the physical migration of these nanoparticles thereby preventing agglomeration and subsequent catalyst deactivation through electrochemical surface area loss.

3.6. Electrochemical activity as analyzed by gas chromatography

The HER and OER processes were upscaled into a two-electrode compartment cell. A cell voltage of 1.68 V was required to maintain a current density of 10 mA cm^{-2} throughout 16 h. The gas sampling from the reactor headspace of the 2-electrode cell was analyzed using a thermal conductivity detector gas chromatography (Agilent 8820 GC system). The GC analysis of the headspace gases showed continuous production of both H_2 and O_2 with a mole ratio of 2:1. Over the 16 h of the two-electrode cell reaction, the reaction showed continuous production of both gases. A faradaic efficiency of 99 % toward HER was determined, with a corresponding turnover frequency (TOF) of 4.55 s^{-1} at an overpotential of 178.6 mV vs RHE towards the formation of hydrogen gas. The high FE is indicative of an electrochemical process centred mostly on the production of hydrogen gas and minimal side reactions. These HER FE and TOF values were significantly higher than those for the NiO/HCS (93%, 1.28s^{-1}) and the CoO/HCS (90.3%, 0.68s^{-1}). Correspondingly, FEs for the OER process and TOFs were determined using the same procedures. The values obtained for the monometallic oxides NiO/HCS (90%, 0.480 s^{-1}) and CoO/HCS (88%, 0.19 s^{-1}) were also smaller than Ni$_x$Co$_{1-x}$O/HCS (99%, 2.78 s^{-1}) indicating faster catalytic HER and OER process on the bimetallic oxide composite. These observations demonstrate the superiority of the bimetallic Ni$_x$Co$_{1-x}$O/HCS electrocatalysts towards the hydrogen evolution reaction compared to the monometallic oxide composites.

3.7. Insights from theoretical calculations

To explore the impact of Co-doping on the electronic properties of NiO structures, we employed Density Functional Theory (DFT) calculations to analyze the density of states (DOS) and partial DOS (PDOS). Fig. 11 illustrates the PDOS, encompassing hybridized Ni 3s, p, and d orbitals, Co 3s, p, and d orbitals, as well as O s and p orbitals. Remarkably, the total DOS maintains an identical shape across Ni$_x$Co$_{1-x}$O/HCS, NiO, and CoO/HCS structures.

All three materials exhibit a structure with a higher total density of states near the Fermi level, indicating improved electrical conductivity for catalytic electron transfer in water-splitting reactions [57]. Notably, the Ni$_x$Co$_{1-x}$O/HCS sample displays a more pronounced Ni p PDOS near the Fermi level compared to NiO/HCS and CoO/HCS. This discrepancy implies diverse electronic interactions with hydrogen evolution reaction (HER) and oxygen evolution reaction (OER) intermediates in the NixCo$_{1-x}$O/HCS sample. The presence of p orbitals in Ni$_x$Co$_{1-x}$O/HCS may play a role in forming oxygen-containing intermediates during OER or in reducing water during HER. Certain p orbitals could exhibit a higher likelihood of participating in relevant redox reactions, influencing the overall catalytic efficiency. Electronic conductivity in transition metal oxides is often associated with the movement of charge carriers, such as electrons or holes, within the material. The increased density of p states may offer additional pathways for electron transport, contributing to enhanced electronic conductivity. This enhanced conductivity is advantageous for efficient charge transfer during electrochemical reactions, explaining the observed superior electrocatalytic water splitting in the bimetallic NixCo$_{1-x}$O/HCS composite. Furthermore, the smaller band gap (0.17 eV) in the NixCo$_{1-x}$O/HCS (Figure SI16) composite,

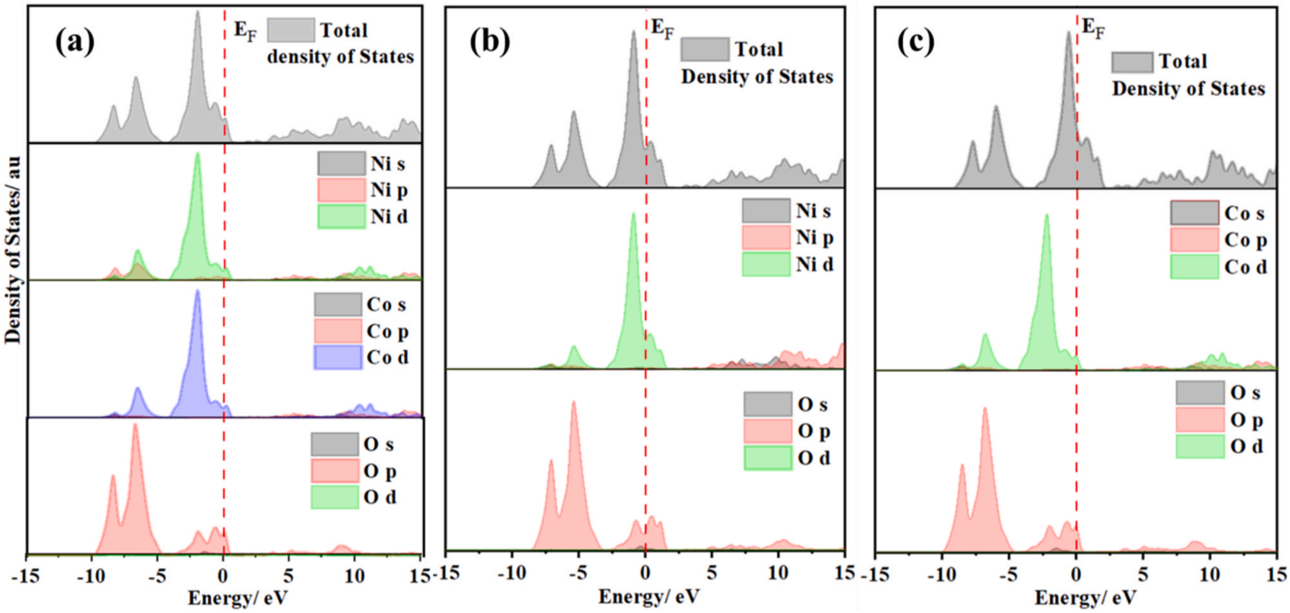

Fig. 11. The DFT calculations showing the total and partial density of states for the (a) NixCo$_{1-x}$O/HCS, (b) NiO/HCS and CoO/HCS.

compared to the 2.07 eV in the CoO/HCS sample (Figure Six), suggests faster electron flow in the bimetallic composite, further supporting its electrocatalytic efficiency.

4. Conclusions

In conclusion, the synthesis of the $Ni_xCo_{1-x}O$/HCS composite yielded a catalyst with outstanding properties in both the HER and OER. Notably, the composite exhibited a low Tafel slope of 68.2 $mVdec^{-1}$ and an overpotential of 178.6 mV to achieve a current density of 10 mA cm^{-2} in HER. Conversely, in OER, the catalysts necessitated an overpotential of 276.4 mV and displayed a Tafel slope of 52.1 $mVdec^{-1}$ for the same current density. In addition, The HER showed faster reaction kinetics through an exchange current density of 0.615 mA cm^{-2} and a charge transfer resistance of 14 Ω, while the OER exhibited an exchange current density of 0.886 mA cm^{-2} and a charge transfer resistance of 10 Ω.

Chronoamperometry over 17 h revealed significant stability in current density for both HER and OER processes. The double layer capacitance of 35.3 mF cm^{-2} indicated the presence of multiple active sites for HER and OER processes.

Microscopy data illustrated the formation of a nanocrystalline catalyst, surpassing monometallic oxides in electrocatalytic performance. The enhanced activity was attributed to the expansion of Ni (111) planes and surface strain in the $Ni_xCo_{1-x}O$ nanoparticles. Additionally, the expanded M – O (Ni–O, Co–O) and M-M (Ni–Ni, Co – Co, Ni–Co) bonds, possibly due to Co or Ni doping, positively influenced intermediates' adsorption and desorption of H_2 and O_2.

Long-term stability was credited to pore confinement of small $Ni_xCo_{1-x}O$ domains within HCS supports and exposure of catalytic active sites through electrochemical degradation of carbon. The bimetallic $Ni_xCo_{1-x}O$/HCS composite catalyst demonstrated superior performance in overall water-splitting, outperforming monometallic NiO/HCS, CoO/HCS, and other reported catalysts. Advanced characterization techniques further supported the catalyst's structural, electronic, and molecular properties, providing insights into its structure-function relationship.

CRediT authorship contribution statement

Victor Mashindi: Conceptualization, Methodology, Investigation, Data curation, Resources, Validation, Visualisation, Formal Analysis, Project Management, Writing, Review and Editing of original draft. **Maxwell W. Terban:** PDF and XRD data Curation, Software, Resources, Visualisation, Formal analysis, Validation, Review, and editing of the original draft. **Debora Motta Meira:** EXAFS Data Analysis. **Beatriz D. Moreno:** XRD data Curation. **Prettier Morongoa:** DFT Data Curation. **Rirhandzu Rikhotso-Mbungela, Genevieve Marx and Jaco Olivier:** TEM Data Curation. **Dean H. Barrett:** Supervision, Conceptualization, Validation, Review and Editing of Original Draft, Resources, Project Management, Funding Acquisition and Project Administration. **Nosipho Moloto:** Supervision, Conceptualization, Resources, Project Management, Funding Acquisition, and Project Administration.

Declaration of competing interest

The authors declare that they have no known competing interests or personal relationships that could have appeared to influence the work reported in this paper.

Acknowledgements

The South Africa National Research Foundation supported this work through the grant holder fund held by Professor Nosipho Moloto, Nedbank, SARChi (South African Research Chairs Initiative) Chair in Energy Materials at the University of the Witwatersrand. Synchrotron data were acquired through South Africa National Research Foundation grant SRUG2204041774 held by Dr Dean H. Barrett, also at the University of the Witwatersrand.

We acknowledge the European Synchrotron Radiation Facility (ESRF) for the provision of synchrotron radiation facilities under proposal MA5435 and the Canadian Light Source under proposals 36G12674 and 37G12950.

Appendix A. Supplementary data

Supplementary data to this article can be found online at https://doi.org/10.1016/j.ijhydene.2024.07.122.

References

[1] Mazloomi K, Gomes C. Hydrogen as an energy carrier: Prospects and challenges. Renew Sustain Energy Rev 2012;16(5):3024–33. https://doi.org/10.1016/j.rser.2012.02.028.

[2] Hasannaeimi V, Mukherjee S. Noble-metal based metallic Glasses as highly catalytic materials for hydrogen oxidation reaction in fuel cells. Sci Rep 2019;9:12136. https://doi.org/10.1038/s41598-019-48582-7.

[3] Liu W, Wan Y, Xiong Y, Gao P. Green hydrogen standard in China: standard and evaluation of low-carbon hydrogen, clean hydrogen, and renewable hydrogen. Int J Hydrogen Energy 2022;47:24584–91. https://doi.org/10.1016/j.ijhydene.2021.10.193.

[4] Luo J, Guo WH, Zhang Q, Wang XH, Shen L, Fu HC, Wu LL, Chen XH, Luo HQ, Li NB. One-pot synthesis of Mn-Fe bimetallic oxide heterostructures as bifunctional electrodes for efficient overall water splitting. Nanoscale 2020;12:19992–20001. https://doi.org/10.1039/d0nr05864e.

[5] Guo Z, Wang X, Yang F, Liu Z. Synergistic effect of Co and Fe bimetallic oxides/hydroxides composite structure as a bifunctional electrocatalyst for enhancing overall water splitting performance. J Alloys Compd 2022;895:162614. https://doi.org/10.1016/j.jallcom.2021.162614.

[6] Tahir A, Arshad F, ul Haq T, Hussain I, Hussain SZ, ur Rehman H. Roles of metal oxide nanostructure-based Substrates in sustainable electrochemical water splitting: recent development and Future Perspective. ACS Appl Nano Mater 2023;6:1631–47. https://doi.org/10.1021/acsanm.2c04580.

[7] Zhou P, Li Z, Zhao Y, Jiang W, Zhao B, Chen X, Wang J, Yang R, Zuo C. Bimetallic and phosphorus-decorated cobalt molybdate nanosheets as highly active bifunctional electrocatalysts for enhanced overall water splitting. Int J Hydrogen Energy 2024;54:1056–64. https://doi.org/10.1016/j.ijhydene.2023.11.282.

[8] Chen Y, Wang J, Yu Z, Hou Y, Jiang R, Wang M, Huang J, Chen J, Zhang Y, Zhu H. Functional group scission-induced lattice strain in chiral macromolecular metal-organic framework arrays for electrocatalytic overall water splitting. Appl Catal, B 2022;307:121151. https://doi.org/10.1016/j.apcatb.2022.121151.

[9] Mashindi V, Mente P, Phaahlamohlaka TN, Mpofu N, Makgae OA, Moreno BD, Barrett DH, Forbes RP, Levecque PB, Ozoemena KI, Coville NJ. Platinum Nanocatalysts supported on Defective hollow carbon spheres: oxygen reduction reaction durability studies. Front Chem 2022;10:839867. https://doi.org/10.3389/fchem.2022.839867.

[10] Coelho AA. TOPAS and TOPAS-Academic: an optimization program integrating computer algebra and crystallographic objects written in C++. J Appl Crystallogr 2018;51:210–8. https://doi.org/10.1107/S1600576718000183.

[11] Leontowich AFG, Gomez A, Moreno BD, Muir D, Spasyuk D, King G, Reid JW, Kim C, Kycia S. The lower energy diffraction and scattering side-bounce beamline for materials science at the Canadian Light Source Leontowich Adam F. G. J Synchrotron Radiat 2021;28:961–9. https://doi.org/10.1107/S1600577521002496.

[12] Juhás P, Davis T, Farrow CL, Billinge SJL. PDFgetX3: a rapid and highly automatable program for processing powder diffraction data into total scattering pair distribution functions. J Appl Crystallogr 2013;46:560–6. https://doi.org/10.1107/S0021889813005190.

[13] Yang X, Juhas P, Farrow CL, Billinge SJL. xPDFsuite: an end-to-end software solution for high throughput pair distribution function transformation, visualization and analysis. J Appl Crystallogr 2014. http://arxiv.org/abs/1402.3163.

[14] Farrow CL, Juhas P, Liu JW, Bryndin D, Bozin ES, Bloch J, Proffen T, Billinge SJL. PDFfit2 and PDFgui: computer programs for studying nanostructure in crystals. J Phys Condens Matter 2007;19:335219. https://doi.org/10.1088/0953-8984/19/33/335219.

[15] Ravel B, Newville M. ATHENA, ARTEMIS, HEPHAESTUS: data analysis for X-ray absorption spectroscopy using IFEFFIT. J Synchrotron Radiat 2005;12:537–41. https://doi.org/10.1107/S0909049505012719.

[16] Clark SJ, Segall MD, Pickard CJ, Hasnip PJ, Probert MI, Refson K, Payne MC. First principles methods using CASTEP. Z für Kristallogr - Cryst Mater 2005;220:567–70. https://doi.org/10.1524/zkri.220.5.567.65075.

[17] Blochl PE. Projector augmented-wave method. Phys Rev B 1994;50:17953. https://doi.org/10.1103/PhysRevB.50.17953.

[18] Monkhorst HJ, Pack JD. Special points for Brillonin-zone integrations. Phys Rev B 1976;13:5188DOI. https://doi.org/10.1103/PhysRevB.13.5188.

[19] Saray MT, Yurkiv V, Shahbazian-Yassar R. Role of kinetics and Thermodynamics in controlling the crystal structure of nickel nanoparticles formed on reduced

graphene oxide: Implications for energy Storage and Conversion Applications. ACS Appl Nano Mater 2023;6:10033–43. https://doi.org/10.1021/acsanm.2c05528.

[20] Wang Z, Li F, Ergang NS, Stein A. Effects of hierarchical architecture on electronic and mechanical properties of nanocast monolithic porous carbons and carbon-carbon nanocomposites. Chem Mater 2006;18:5543–53. https://doi.org/10.1021/cm062050u.

[21] Ferrari AC, Robertson J. Interpretation of Raman spectra of disordered and amorphous carbon. Phys Rev B 2000;61:14095. https://doi.org/10.1103/PhysRevB.61.14095.

[22] Dantas S, Struckhoff KC, Thommes M, Neimark AV. Phase behaviour and capillary condensation hysteresis of carbon Dioxide in Mesopores. Langmuir 2019;35:11291–8. https://doi.org/10.1021/acs.langmuir.9b01748.

[23] Mashindi V, Mente P, Mpofu N, Phaahlamohlaka TN, Makgae ON, Kirkland AI, Forbes R, Ozoemena KI, Levecque PB, Coville NJ. Platinum supported on pristine and nitrogen-doped bowl-like broken hollow carbon spheres as oxygen reduction reaction catalysts. J Appl Electrochem 2021;51:991–1008. https://doi.org/10.1007/s10800-021-01554-0.

[24] Chen X, Wang X, Fang D. A review on C1s XPS-spectra for some kinds of carbon materials. Fullerenes, Nanotub Carbon Nanostruct 2020;28:1048–58. https://doi.org/10.1080/1536383X.2020.1794851.

[25] Cheng CYH, Zheng L, Lin J, Xu Q, Qiu Y, Pan Z, Qiu Y. Tailoring metal-oxygen bonds Boosts oxygen reaction kinetics for high-performance Zinc-air Batteries. Nano Lett 2023;23:1573–81. https://doi.org/10.1021/acs.nanolett.3c00053.

[26] Gromov DG, Pavlova LM, Savitsky AI, Trifonov AY. Nucleation and growth of Ag nanoparticles on amorphous carbon surface from vapor phase formed by vacuum evaporation. Appl Phys Mater Sci Process 2015;118:1297–303. https://doi.org/10.1007/s00339-014-8834-0.

[27] Brandiele R, Parnigotto M, Mazucatto M, Dalconi MC, Bertolotti F, Ricci GA, Sasso GD, Durante C. The interplay between surface area and sulfur doping of carbon support on Pt NPs nucleation and growth: a synergistic enhancement of catalytic activity for oxygen reduction. Appl Catal, B: Environment and Energy 2024;344:123620. https://doi.org/10.1016/j.apcatb.2023.123620.

[28] Lagarteira T, Delgado S, Garcia GP, Ortiz A, Mendes A. Oxygen reduction stability of graphene-supported electrocatalyst: electrochemical and morphological evidence. Int J Hydrogen Energy 2023;48:20901–13. https://doi.org/10.1016/j.ijhydene.2023.03.359.

[29] Kandel MR, Pan UN, Dhakal PP, Ghising RB, Nguyen TT, Zhao J, Kim NH, Lee JL. Unique heterointerface engineering of Ni_2P-MnP nanosheets coupled Co2P nanoflowers as hierarchical dual-functional electrocatalyst for highly proficient overall water-splitting. Appl Catal, B 2023;331:122680. https://doi.org/10.1016/j.apcatb.2023.122680.

[30] Christiansen TL, Cooper SR, Jensen KMO. There's no place like real space: Elucidating size-dependent atomic structure of nanomaterials using pair distribution function analysis. Nanoscale Adv 2020;2:2234–54. https://doi.org/10.1039/d0na00120a.

[31] Keen DA. Total scattering and the pair distribution function in crystallography. Crystallogr Rev 2020;26:141–99. https://doi.org/10.1080/0889311X.2020.1797708.

[32] Rodenbough PP, Zheng C, Liu Y, Hui C, Xia Y, Ran Z, Hu Y, Chan S. Lattice expansion in metal oxide nanoparticles: MgO, Co_3O_4, & Fe_3O_4. J Am Ceram Soc 2017;100:384–92. https://doi.org/10.1111/jace.14478.

[33] Jain A, Ong SP, Hautier G, Chen W, Richards WD, Dacek S, Cholia S, Gunter D, Skinner D, Ceder G, Persson KA. Commentary: the materials project: a materials genome approach to accelerating materials innovation. Apl Mater 2013;1:011002. https://doi.org/10.1063/1.4812323.

[34] Yin J, Jin J, Liu H, Huang B, Lu M, Li J, Liu H, Zhang H, Peng Y, Xin P, Peng H, Xi P, Yan C. $NiCo_2O_4$-Based nanosheets with uniform 4 nm Mesopores for excellent Zn–air Battery performance. Adv. Mater. 2020;32:2001651. https://doi.org/10.1002/adma.202001651.

[35] Zhang J, Qian J, Ran J, Xi P, Yang L, Gao D. Engineering lower coordination atoms onto NiO/Co_3O_4 Heterointerfaces for boosting oxygen evolution reactions. ACS Catal 2020;10:12376–84. https://doi.org/10.1021/acscatal.0c03756.

[36] Zhai W, Chen Y, Liu Y, Sakthivel T, Ma Y, Guo S, Qu Y, Dai Z. Bimetal-incorporated black Phosphorene with surface electron Deficiency for efficient Anti-Reconstruction water electrolysis. Adv Funct Mater 2023;33:2301565. https://doi.org/10.1002/adfm.202301565.

[37] Sun J, Yang H, Gao W, Cao T, Zhao G. Diatomic Pd−Cu metal-phosphorus sites for complete N≡N bond formation in Photoelectrochemical nitrate reduction. Angew Chem 2022;61:e202211373. https://doi.org/10.1002/anie.202211373.

[38] Zhang H, Yao T, Sun Z, Li Y, Liu Q, Hu F, Pan Z, He B, Xie Z, Wei S. Structural study on Co-Ni bimetallic nanoparticles by X-ray spectroscopy. J Phys Chem C 2010;114:13596–600. https://doi.org/10.1021/jp105080t.

[39] Song C, Tayal A, Seo O, Kim J, Chen Y, Hiroi S, Kumara LSR, Kusada K, Kobayashi H, Kitagawa H, Sakata O. Correlation between the electronic/local structure and CO-oxidation activity of Pd: Xru_{1-x} alloy nanoparticles. Nanoscale Adv 2019;1:546–53. https://doi.org/10.1039/c8na00305j.

[40] He Q, Li J, Qiao Y, Zhan S, Zhou F. Investigation of two-electron ORR pathway of non-metallic carbon-based catalysts with P-C bond structure in Cl-bearing electrolytes. Appl Catal, B 2023;339:123087. https://doi.org/10.1016/j.apcatb.2023.123087.

[41] Nikolic VM, Maslovara S, Tasic GS, Brdaric TP, Lauservic P, Radac BB, Kaninski MPM. Kinetics of hydrogen evolution reaction in alkaline electrolysis on a Ni cathode in the presence of Ni-Co-Mo based ionic activators. Appl Catal, B 2015;179:88–94. https://doi.org/10.1016/j.apcatb.2015.05.012.

[42] Manoj B, Duy TT, Sampath P, Do HK, Nam HK, Joong HL. Continuously interconnected network enabled by Pt single atoms-promoted CoNiP-CoNi heterostructures for efficient water electrolysis. Nano Energy 2024;123:109413.

[43] Jyothirmai MV, Dantuluri R, Sinha P, Abraham BM, Singh JK. Machine-learning-driven high-throughput Screening of transition-metal atom Intercalated g-C_3N_4/MX_2 (M = Mo, W; X = S, Se, Te) heterostructures for the hydrogen evolution reaction. ACS Appl Mater Interfaces 2024;16(10):12437–45.

[44] Maziyar K, Mohammad Z, Hassan A, Mehdi B, Marzieh N, Javad B, Navid R. Toward preparation of large scale and uniform mesoporous $BiVO_4$ thin films with enhanced photostability for solar water splitting. J Alloys Compd 2023;969:172409.

[45] Qiu Z, Ma Y, Edvinsson T. In operando Raman investigation of Fe doping influence on catalytic NiO intermediates for enhanced overall water splitting. Nano Energy 2019;66:104118. https://doi.org/10.1016/j.nanoen.2019.104118.

[46] Cao X, Medvedeva JE. Copper cobalt Selenide as a high-efficiency bifunctional electrocatalyst for overall water splitting: combined experimental and Theoretical study. ACS Appl Energy Mater 2020;3:3092–103. https://doi.org/10.1021/acsaem.0c00262.

[47] Chen A, Lu J, Zhu H, Zhang H, Zeng Z, Zheng L, Liang H. Construction of highly durable electrocatalysts by pore confinement and anchoring effect for the oxygen reduction reaction. New J Chem 2022;46:7253–562. https://doi.org/10.1039/d1nj06098h.

[48] Yang L, Li H, Yu Y, Wu Y, Zhang L. Assembled 3D MOF on 2D nanosheets for Self-boosting catalytic synthesis of N-doped carbon Nanotube encapsulated metallic Co electrocatalysts for overall water splitting. Appl Catal, B 2020;271:118939. https://doi.org/10.1016/j.apcatb.2020.118939.

[49] Li A, Zhang L, Wang F, Zhang L, Li L, Chen H, Wei Z. Rational design of porous Ni-Co-Fe ternary metal phosphides nanobricks as bifunctional electrocatalysts for efficient overall water splitting. Appl Catal, B 2022;310:121353. https://doi.org/10.1016/j.apcatb.2022.121353.

[50] Liu B, Li S, Wang T, Yang Y, Wang L, Zhang X, Liu Z, Niu L. Construction of CoFe bimetallic phosphide microflowers electrocatalyst for highly efficient overall water splitting. Catal Commun 2023;175:106607. https://doi.org/10.1016/j.catcom.2023.106607.

[51] Wang S, Zhang Y, Deng X, Ma Z, Cheng R, Wan Z, Li J, Wang X. Rational construction of loosely packed nickel nano particulates with residual HCOO ligands derived from a Ni-MOF for high-efficiency electrocatalytic overall water splitting. J. Mater. Chem. A. 2023;11:5222–32. https://doi.org/10.1039/d2ta09369c.

[52] Yao L, Li R, Zhang H, Humayun M, Xu X, Fu Y, Nakiforov A, Wang C. Interface engineering of NiTe@CoFe LDH for highly efficient overall water-splitting. Int J Hydrogen Energy 2022;47:32394–404. https://doi.org/10.1016/j.ijhydene.2022.07.135.

[53] Dai Z, Du X, Zhang X. The synthesis of Ni-Co-Fe-Se@NiCo-LDH nanoarrays on Ni foam as efficient overall water splitting electrocatalyst. J Alloys Compd 2023;946:169451. https://doi.org/10.1016/j.jallcom.2023.169451.

[54] Wu J, Chen W, Zheng H, Chen M, Xia J, Qian X. Hierarchical core-shell structural $Ni_2P/NiMoO_4$ @CoP/FeP_2 nanorods as difunctional electrocatalysts for efficient overall water splitting. J Alloys Compd 2023;945:169357. https://doi.org/10.1016/j.jallcom.2023.169357.

[55] Yu X, Yu Z, Zhang X, Li P, Sun B, Gao X, Yan K, Liu H, Duan Y, Gao M, Wang G, Yu S. Highly disordered cobalt oxide nanostructure induced by sulfur incorporation for efficient overall water splitting. Nano Energy 2020;71:104652. https://doi.org/10.1016/j.nanoen.2020.104652.

[56] Jiang Z, Jing M, Feng X, Xiong J, He C, Douthwaite M, Zheng L, Song W, Liu J, Qu Z. Stabilizing platinum atoms on CeO_2 oxygen vacancies by metal-support interaction induced interface distortion: mechanism and application. Appl Catal, B 2020;278:119304. https://doi.org/10.1016/j.apcatb.2020.119304.

[57] Wang X, Xie J, Li S, Yuan Z, Sun Y, Gao X, Teng Z, Zhang H, Li J, Wang S, Yang Z, Yan Y. Enhancing interfacial electric field in WO_3-C_3N_4 through fermi level modulation for electrocatalytic nitrogen reduction. Appl Catal, B 2023;339:123126. https://doi.org/10.1016/j.apcatb.2023.123126.